

Aperiodic nano-photonic design

Ioan L. Gheorma,¹ Stephan Haas,² and A. F. J. Levi^{1,2}

¹*Department of Electrical Engineering,*

University of Southern California, Los Angeles, CA, 90089-2533

²*Department of Physics and Astronomy,*

University of Southern California, Los Angeles, CA, 90089-0484

Abstract

The photon scattering properties of aperiodic nano-scale dielectric structures can be tailored to closely match a desired response by using adaptive algorithms for device design. We show that broken symmetry of aperiodic designs provides access to device functions not available to conventional periodic photonic crystal structures.

PACS numbers: 42.70.Qs, 02.60.Pn, 11.80.La

Keywords: adaptive algorithm, optimization, aperiodic, photonic crystal, scattering

A. Introduction

The spatial arrangement of nano-scale dielectric scattering centers embedded in an otherwise uniform medium can strongly influence propagation of an incident electromagnetic wave. Exploiting this fact, we iteratively solve an inverse problem [1] to find a spatial arrangement of identical non-overlapping scattering centers that closely matches a desired, or target, response. Of course, the efficiency of adaptive algorithms used to find solutions may become an increasingly critical issue as the number of scattering centers, N , increases. However, even for modest values of N , this method holds the promise of creating nano-phonic device designs that outperform conventional approaches based on spatially periodic photonic crystal (PC) structures.

The configurations considered by us consist of either lossless dielectric rods in air or circular holes in a dielectric similar to the majority of quasi two dimensional (2D) PCs reported in the literature by, for example, [2, 3]. To confirm the validity of our 2D simulations we compare the optimized configuration with full three dimensional (3D) simulations.

B. Calculation of the scattered field

The optimization process is an iterative procedure, in which the scattered field from a trial configuration of cylindrical rods or circular holes is compared with that of the target. We note that computation of the scattered field is sometimes referred to as the forward problem.

The electromagnetic field solver used is based on the analytical solution of the Helmholtz equation by separation of variables in polar coordinates. A typical problem we consider is a set of N long, parallel, lossless circular dielectric rods distributed in a uniform medium and illuminated by an electromagnetic wave perpendicular to the axis of the cylinders. The natural geometry of the system led us to use a 2D electromagnetic field solver. When analyzing scattering from one cylinder, the solution, expressed as a Fourier-Bessel series, is found immediately by imposing the continuity of the electric and magnetic field components at the rod surface. However, when studying scattering from two or more cylinders, multiple scattering gives an additional linear system that has to be solved in order to find the Fourier-Bessel coefficients [4]. For a given number of Bessel functions used this linear system has a

reduced form which is conveniently described using the scattering matrix method [5, 6, 7, 8, 9]. The input wave can, in principle, be of arbitrary shape so long as it is expressed as a Fourier-Bessel series. In our simulations the input beam is a gaussian and both TE and TM polarizations are considered. The calculated Fourier-Bessel coefficients for the gaussian beam conform [10, 11]. Additional details on the electromagnetic solver used may be found in Appendix A.

C. Optimization

For the results presented in this paper, the optimization method used is the guided random walk. The positions of individual cylinders are randomly changed by a small amount, the modified distribution is simulated, and if the result is closer to the target function, such that the error defined in Appendix B is decreased, then the new configuration is accepted, otherwise it is rejected. The actual implementation of the adaptive algorithm also includes other types of collective motion such as moving more than one cylinder per iteration, and moving or rotating all the cylinders.

In general the target function may be any electromagnetic distribution. A typical target function might involve redirecting and reshaping the input beam. More complex situations involving optically active materials are not considered in this paper. Because the target function can specify the field distribution of a guided mode, it is possible to create mode converters to interface between a fiber or ridge waveguide and a PC waveguide. In this paper we report on redirecting and reshaping an electromagnetic beam using optimized aperiodic nano-structures.

D. Results

To illustrate our approach, we considered an input beam of gaussian profile scattered by an angle of 45° . The target functions we consider are a top hat distribution of the optical intensity with respect to the scattering angle and a cosine squared (\cos^2) distribution of the intensity. We note that a modal field distribution target function requires amplitude and phase to be specified.

As an initial demonstration we chose the top-hat intensity function because it is difficult

to achieve (even approximately) in conventional optical systems and serves to show the capabilities of our adaptive algorithm. Application of such an intensity distribution includes guaranteeing uniform illumination of the active area of a photodetector. On the other hand the \cos^2 intensity distribution target approximates the transverse spatial mode intensity typically found in a waveguide and so could be considered a first step toward design of a waveguide coupler.

1. *Top-hat target function*

Optimization of a top-hat intensity distribution target function is performed starting from a configuration of $N = 56$ dielectric rods (represented in Fig. 1(a) by the small circles), each having refractive index $n = 1.5$, and diameter $d = 0.4 \mu\text{m}$. The medium surrounding the rods is air and the structure is illuminated by a TM polarized (electric field along the z direction) gaussian beam of width $2\sigma = 4 \mu\text{m}$, wavelength $\lambda = 1 \mu\text{m}$, and propagating along the positive x direction (from left to right in Fig. 1(a)). The initial configuration of the rods and intensity distribution are illustrated in Fig. 1(a), where the arrows represent (in arbitrary units) the real part of the Poynting vectors. The target function window (represented in Fig. 1(a) by a missing arc in the $7 \mu\text{m}$ radius observation circle) extends from 30° to 60° . Fig. 1 (b) shows normalized intensity (real part of the normal component of total field Poynting vectors directed outwards) as a function of angle on a radius of $7 \mu\text{m}$ from the center of the symmetric array. Clearly, for the initial configuration, the overlap with the top-hat target function (broken line) is poor.

Fig. 2(a) shows the spatial distribution of the $N = 56$ rods with the real part of Poynting vectors after 9700 iterations of the adaptive search algorithm. Fig. 2(b) shows the corresponding angular distribution of the intensity. In Fig. 2(c) the distribution of the electric field (relative magnitude, with 1 corresponding to the maximum magnitude in the incident gaussian beam) is shown and in Fig. 2(d) the relative error versus number of iterations (the errors are normalized with respect to the initial value) are represented. Note that for this system with $2 \times N$ positional degrees of freedom, the error is not saturated even after 9,700 iterations (Fig. 2(d)) and the structure can be further optimized by performing additional iterations. The error is computed using the method described in Appendix B with exponent $\gamma = 2$ on the observation circle of radius $7 \mu\text{m}$.

For comparison, in Fig. 3 we show the results of using a PC with the same number of dielectric rods, $N = 56$. Clearly, the number of rods is not sufficient to redirect all the beam in the 45° ($\pm 15^\circ$) direction and the error with respect to the target function is unacceptably large. The spatial symmetry of the PC excludes access to the top-hat target function. It is only by breaking the symmetry that one may acquire the target. In general, broken symmetry enables functionality.

2. Cosine squared target function

For a \cos^2 target function we chose a different situation in which there are $N = 26$ lower index cylinders (SiO_2 , $n = 1.45$) embedded in a higher index material (Si, $n = 3.5$). The 3D equivalent of the modelled situation is a Si slab with cylindrical perforations embedded in SiO_2 . The incident wave is a TE polarized (magnetic field along the z direction) gaussian beam of width $2\sigma = 1.5 \mu\text{m}$ and wavelength $\lambda = 1.5 \mu\text{m}$. In a similar manner to the previous example, the initial configuration and intensity distribution are illustrated in Fig. 4. The back scattered intensity in the input region is calculated as the difference between the incident field Poynting vector and total field Poynting vector. In Fig. 5 we show the optimized configuration, Poynting vectors, relative error versus number of iterations, and relative magnitude of the magnetic field (with 1 corresponding to the maximum magnitude in the original gaussian beam). This time the position of the $N = 26$ cylinders could be changed and so could their diameters d , giving a total number of degrees of freedom that is three times the number of cylinders N . The values of the diameters are constrained to the range $0.2 \leq d \leq 0.5 \mu\text{m}$. The error is computed using the metric from Appendix B with exponent $\gamma = 1$ on a $6 \mu\text{m}$ radius circle. Notice that due to the small number of cylinders the actual number of degrees of freedom is smaller (78) relative to the previous calculations with a top-hat target function (112) and the optimization saturates after a comparatively small number of iterations.

3. Computing resources

Our previous optimization work on 1D problems [12] required relatively insignificant computational resources. Optimization algorithms using 2D electromagnetic solvers are

always more compute intensive than those for 1D structures. Interesting simulations in 3D are even more compute intensive and often require parallel computing. Each of the simulations (top-hat and \cos^2 target) discussed in this paper took 4 days to complete (9,700 iterations in the first case and 7,600 of the second) using a Pentium IV processor with a 3 GHz clock frequency, 533 MHz memory bus, and 1 GB RDRAM.

The compute time for the forward problem solver is dominated by the solution of a linear system with a full matrix of complex numbers and thus is strongly dependent on the number of cylinders N considered in the problem and the number of Bessel functions N_b used. The size of the system is $N_m = N(2N_b + 1)$ and the solver routine (iteratively corrected LU decomposition [13]) time is proportional to the cube of the matrix size ($O(N_m^3)$). When using an incident plane wave or a cylindrical wave the number of Bessel functions needed is very small, however, an appropriately accurate approximation of the gaussian beam shape requires a large number of Bessel functions and a corresponding increase in compute time.

4. Comparison with 3D Simulation

For practical purposes, a comparison with 3D electromagnetic simulations serves to confirm the accuracy of solutions obtained with the 2D simulator. Also, since 3D simulations are much more time consuming than 2D ones, one might adopt the 2D optimization result as a starting point for a limited number of 3D iterations which are then used to further refine optimization.

In this paper we compare results of our 2D electromagnetic simulations with 3D Finite Integration Technique (FIT) simulations obtained using a commercially available package, CST Microwave Studio [14].

In a realistic structure one might anticipate the infinitely long cylindrical hole structure used in the \cos^2 target simulation to be replaced with SiO_2 filled holes in a Si slab itself embedded in SiO_2 . The input beam might be launched into this slab from a ridge waveguide. In our simulations, the wavelength of the light is $\lambda = 1.5 \mu\text{m}$ and the polarization is TE. The Si slab is $0.6 \mu\text{m}$ thick and the effective index of the fundamental mode of this slab waveguide is the same as the index of the material surrounding the cylinders in the 2D simulation. The diameter of the holes is $d = 0.4 \mu\text{m}$ and the mode size of the ridge waveguide (Fig. 6) is approximately $1.5 \mu\text{m}$ and so the same as the width of the gaussian beam used for the 2D

simulations. The differences between the two simulations (Fig. 6(b) for the 3D and Fig. 6(d) for the 2D simulation results) are primarily due to the nonuniformity of the field and structure in the z direction but also because of the difference between the gaussian beam and the ridge mode and the fundamentally 3D discontinuity between the ridge waveguide and the slab. These differences translate into a 30% decrease in peak intensity and 25% decrease in the total power directed in the desired direction for the 3D simulation compared to the 2D one (Fig. 6 (c)).

5. Sensitivity analysis

We analyzed the influence of small changes in the wavelength of the incident beam on error. We took the optimized configuration from the \cos^2 target example (Fig. 5(a)) and simulated the effect of changing the frequency of the input light. The relative deviation from the minimum error is shown in Fig. 7 as a function of the electromagnetic wave frequency shift. Frequency variations of $\Delta f = 200$ GHz only change the error by 0.3% of its minimum value. Thus an optical beam centered at wavelength $\lambda = 1.5 \mu\text{m}$ modulated at very high speed will behave essentially as the simulated monochromatic wave at $\lambda = 1.5 \mu\text{m}$ (200 THz). Even a 1 THz deviation in frequency changes the error by only 6 – 7 %.

Another important issue is the sensitivity of the aperiodic nano-photonics design to variations and errors introduced by the fabrication process. As an initial study we explored the sensitivity of the design to changes in the position of the cylinders. Other parameters that are influenced by fabrication processes such as the diameter and detailed shape of the cylinders, index of refraction, direction of the input ridge waveguide with respect to the cylinders, etc., are not analyzed in this paper.

To estimate the sensitivity to position, for the same \cos^2 target function example, we use the following method. First, one by one the cylinders are displaced by a small fixed distance Δ in the positive and negative x and y directions and the change in error is evaluated for each cylinder (the maximum error created out of the 4 displacements). The displacement values used are small compared to the initial diameters of the cylinders ($d = 400$ nm). Five values for the displacement Δ are considered: 10, 20, 30, 40, and 50 nm. Next the 10 displaced cylinders with the greatest influence on the error are selected. These cylinders, as expected, are located in regions associated with high field intensity.

The selected cylinders are all individually moved randomly by the same step size in the positive and negative x and y directions (each movement has the same $1/4$ probability). The movement of each cylinder is independent of the movements of the other selected cylinders. This way we generate a number of slightly modified configurations. The errors for 10 of these modified configurations are computed for each displacement value and a combined plot generated (Fig. 8).

We chose this very simplified method for estimating the sensitivity to position because a more complete approach would involve independent displacements of each cylinder in completely random directions and with variable distances and hence give rise to significant computational effort. The plot in Fig. 8, suggests that 10 nm precision in fabrication might be needed to ensure less than 10% increase in minimum error for devices operating at wavelength $\lambda = 1.5 \mu\text{m}$.

6. *Comparison with photonic crystal inspired devices*

In recent years, spatially periodic dielectric structures have been studied and applied to both optics and microwaves [15, 16, 17]. It has been shown that introduction of point and line defects in PCs can be used to filter, demultiplex, and guide electromagnetic waves [2, 3, 18, 19]. However, there are numerous unresolved design issues with PC inspired devices that limit prospects of adoption as practical components. For example, when coupling between standard fibers or waveguides and PC waveguides, the back reflection is either unacceptably large [20] or requires use of relatively large coupling regions [21, 22]. As another example, it is well known that the necessarily finite size of the PC can have a dramatic and detrimental impact on device performance [23]. Solutions to these and similar problems are stymied by the limited number of degrees of freedom inherent to PC design. Rather than struggle for solutions within the constraints of spatial symmetry imposed by PC structures, our approach is based on breaking the underlying spatial symmetries and thereby exposing larger numbers of degrees of freedom with which to design and optimize nano-photonic devices.

Our experience so far indicates that optimization of such systems is best achieved using numerical adaptive design techniques. This is because solutions, such as that illustrated in Fig. 5, have such a high degree of broken symmetry it is unlikely analytic methods or

conventional intuition could usefully be applied.

7. Conclusions

In this paper we have shown that aperiodic nano-photonic dielectric structures designed using adaptive algorithms can be tailored to closely match desired electromagnetic transmission and scattering properties. It is the broken symmetry of the structure that allows more degrees of freedom and the possibility of better optimization compared to symmetric photonic crystal structures.

In general the frequency response and spatial response of this system can have very complicated forms. It is the large number of degrees of freedom that allow us to tailor the response to the desired target. The configuration space is even more complex if materials with optical loss or gain are considered.

Acknowledgments

We thank P. B. Littlewood for helpful comments. This work is supported in part by DARPA.

APPENDIX A: ELECTROMAGNETIC SOLVER

For brevity we will only discuss TM polarized electromagnetic waves. For the TE case the equations are similar with H replacing E . The total field is written as the sum of the incident field E_{inc} and the field E_{sc} scattered from the cylinders $E = E_{inc} + \sum_{i=1}^N E_{sc}^i$. The actual incident field on a cylinder labeled with index j is $E_{inc}^j = E_{inc} + \sum_{i \neq j}^N E_{sc}^i$ [4, 9]. We are interested in solving the Helmholtz equation for the total field, $\nabla^2 E + k^2 E = 0$, where $k = k_0$ in the region outside the cylinders and $k = k_1$ inside the cylinders. The method used to solve this equation is separation of variables in polar coordinates. Of course, the solution of the homogeneous Helmholtz equation in polar coordinates is well known. All field quantities may be written in the form of Fourier-Bessel series with the coefficients α_m and β_m determined from the boundary conditions. Hence, $E = \sum_{m=-\infty}^{\infty} \alpha_m Z_m(k\rho) e^{im\theta} + \sum_{m=-\infty}^{\infty} \beta_m \tilde{Z}_m(k\rho) e^{im\theta}$, where Z_m and \tilde{Z}_m are two conjugate cylindrical functions. These

functions are either the first order Bessel functions J_m and Y_m or the second order Bessel functions (Hankel functions) $H_m^{(1)}$ and $H_m^{(2)}$. The pair chosen depends on the boundary conditions. Outside the cylinders the asymptotic behavior determines which functions are used. Since only the $H_m^{(2)}$ function has the behavior of an out-propagating cylindrical wave, the field of the scattered wave E_{sc} has to be written using only $H_m^{(2)}$ of the $\{H_m^{(1)}, H_m^{(2)}\}$ pair. Hence the scattered field is $E_{sc} = \sum_{m=-\infty}^{\infty} b_m H_m^{(2)}(k_0 \rho) e^{im\theta}$. Inside the cylinders we have to choose the $\{J_m, Y_m\}$ pair because the Hankel functions are both singular at the origin. This behavior comes from the Y_m part of the Hankel function ($H_m^{(1)} = J_m + iY_m$, $H_m^{(2)} = J_m - iY_m$) and thus only the J_m functions can be kept for the interior. In this case the total internal field is $E_{tot}^{int} = \sum_{m=-\infty}^{\infty} a_m J_m(k_1 \rho) e^{im\theta}$.

After expressing the incident field in polar coordinates, i.e. in a Fourier-Bessel series, we can write the electric and magnetic field continuity conditions at the boundaries of each cylinder. This gives us a system of equations with the unknowns being the Fourier-Bessel coefficients of the scattered field outside the cylinders and total field inside the cylinders. The system can be simplified by using the relationship between the Bessel-Fourier coefficients of a field incident on a cylinder and the coefficients for the scattered and internal fields [5, 6, 7, 8].

APPENDIX B: ERROR FUNCTION

The optimization is based on the minimization of a functional, which is defined as the residual error between the calculated angular distribution of the normal component of the Poynting vector \mathbf{S} and a distribution expressed as a target function. This error function is computed starting from the difference in intensity between the target and the result. In 2D the error is calculated along an observation line (often a circle around the group of cylinders). This line is divided into small portions and the normal component of the \mathbf{S} vector is calculated in the center of each segment.

Let the target function $T(\alpha)$ be the angular distribution of intensity exiting the circular observation region and $S_n(\alpha)$ the normal component of the real part of the Poynting vector ($S_n(\alpha) = \mathbf{S}(\alpha) \cdot \mathbf{n}(\alpha)$ where \mathbf{n} is the normal unit vector). In this space of functions defined on $[0^\circ, 360^\circ]$ and having real values we can define a "distance" D between result $S_n(\alpha)$ and target $T(\alpha)$ as $D = \frac{1}{2\pi} \int_0^{2\pi} |S_n(\alpha) - T(\alpha)|^\gamma d\alpha$. To properly evaluate the difference between

the target and result the functions T and S and have to be similarly normalized.

In general, the exponent γ can take any value. Choosing $\gamma = 1$ assures that each improvement is considered with the same weight. When choosing $\gamma > 1$ improvements made in regions where the target and the results are very different influence the integral D more than a few smaller improvements in other regions. This means that $\gamma = 1$ tends to ensure an uniform convergence while $\gamma > 1$ favors reduction of major differences between target and result. The greater the numerical value of γ , the more important this effect becomes, while for $0 < \gamma < 1$ the effect is reversed. And finally, a negative exponent γ tends to push the solution further away from the target, in a manner which depends on the numerical value of γ .

One could use different exponents for different stages of the iterative process. For example $\gamma = 1$ could be used at the beginning of the convergence procedure to avoid local minima. Later, the value of γ could be increased to accelerate convergence towards a minimum. Furthermore, if one decides that this minimum is not sufficiently close to the target function, application of a negative exponent would divert the iterations from this local minimum to some intermediate point were $\gamma > 1$ iterations could be restarted in the search for a better minimum.

We use the real part of the Poynting vector in our calculation of $S_n(\alpha)$. For most scattering directions this is the Poynting vector of the total field, with the exception of the input beam region where we use the scattered field in the first example (the top-hat target function) and the difference between the Poynting vector of the input field and total field in the second example (the \cos^2 target function).

The distances, or errors, D are computed numerically by dividing the observation circle into very small and equal portions and the integral replaced by a sum over these portions $D^* = \sum_{i=0}^{N_p} \left| \frac{S_n(\alpha_i)}{N_s} - \frac{T(\alpha_i)}{N_t} \right|^\gamma$ where N_s and N_t are normalization factors. Different normalization methods can be used such as normalization to the maximum value, normalization to the sum of all values, or normalization to the sum of the squares. Since in our case the functions involve intensity we have chosen the normalization to be the sum *i.e.* the total power.

Although not used in this paper, it is worth mentioning that when optimizing for a modal shape distribution (both amplitude and phase) a better choice for error function would be the overlap integral between the actual field distribution and the desired modal

field distribution. In this situation the target would be maximized.

- [1] The problem considered here differs somewhat from conventional inverse problems which usually involve calculations on experimentally measured data.
- [2] J. Smajic, C. Hafner, and D. Erni, *Opt. Expr.* **11**, 1378(2003).
- [3] S. Fan, S. G. Johnson, J. D. Joannopoulos, C. Manolatu, and H. A. Haus, *J. Opt. Soc. Am. B* **18**, 162 (2001).
- [4] D. Felbacq, G. Tayeb, and D. Maystre, *J. Opt. Soc. Am. A* **11**, 2526(1994).
- [5] G. Guida, D. Maystre, G. Tayeb, and P. Vincent, *J. Opt. Soc. Am. B* **15**, 2308 (1998).
- [6] G. Tayeb and D. Maystre, *J. Opt. Soc. Am. A* **14**, 3323 (1997).
- [7] B. Gralak, S. Enoch and G. Tayeb, *J. Opt. Soc. Am. A* **17**, 1012 (2000).
- [8] J. Yonekura, M. Ikeda, and T. Baba, *IEEE J. Lightwave Tech.* **17**, 1500 (1999).
- [9] B. C. Gupta and Z. Ye, *J. Appl. Phys.* **94**, 2173 (2003).
- [10] S. Kozaki, *J. Appl. Phys.* **53**, 7195 (1982).
- [11] Z. Wu and L. Guo, *PIER* **18**, 317 (1998).
- [12] Yu Chen, R. Yu, W. Li, O. Nohadani, S. Haas, and A. F. J. Levi, *J. Appl. Phys.*, unpublished.
- [13] W. H. Press, S. A. Teukolsky, W. T. Vetterling, and B. P. Flannery, "Numerical Recipes", Cambridge University Press, Cambridge, 2002.
- [14] <http://www.cst.de/>
- [15] J. D. Joannopoulos, R. D. Meade, and J. N. Winn, "Photonic Crystals", Princeton Univ. Press, Princeton, NJ, 1995
- [16] C. A. Kyriazidou, H. F. Contopanagos, and N. G. Alexopoulos, *IEEE Trans. Microwave Theory Tech.* **49**, 297 (2001).
- [17] F. Gadot, et. al., *IEEE Trans. Magn.* **34**, 3028 (1998).
- [18] M. Koshiba, *IEEE J. Lightwave Tech.* **19**, 1970 (2001).
- [19] S. Fan, H. Haus, P. Villeneuve, and J. Joannopoulos, *Opt. Expr.* **3**, 4 (1998).
- [20] T. D. Happ, M. Kamp, and A. Forchel, *Opt. Lett.* **26**, 1102 (2001).
- [21] A. Mekis and J. D. Joannopoulos, *IEEE Journ. Lightwave Tech.* **19**, 861 (2001).
- [22] Y. Xu, R. K. Lee, and A. Yariv, *Opt. Lett.* **25**, 755 (2000).
- [23] Y-H. Ye, D.-Y. Jeong, T. S. Mayer, and Q. M. Zhang, *Appl. Phys. Lett.* **82**, 2380 (2003).

FIG. 1: Starting configuration for the top-hat target function example. 56 dielectric rods with diameter $d = 0.4 \mu\text{m}$, index $n = 1.5$, in air. The incident beam, which propagates along the x axis (left to right), is a TM polarized gaussian beam with beamwidth $2\sigma = 4 \mu\text{m}$, and wavelength $\lambda = 1 \mu\text{m}$. (a) Positions of the cylinders and distribution of the Poynting vector field. The observation circle, has a radius of $7 \mu\text{m}$ and it is represented without the target window between 30 and 60 degrees. (b) Computed angular intensity distribution (continuous line) at radius $7 \mu\text{m}$ compared with the target distribution (dashed line).

FIG. 2: Optimized configuration for the top-hat target function example. 56 dielectric rods with diameter, $d = 0.4 \mu\text{m}$, index $n = 1.5$, in air. TM polarization gaussian beam with incident beamwidth $2\sigma = 4 \mu\text{m}$, and wavelength $\lambda = 1 \mu\text{m}$. (a) Positions of the cylinders and distribution of the Poynting vector field after 9,700 iterations. The observation circle, has a radius of $7 \mu\text{m}$ and it is represented without the target window between 30 and 60 degrees. (b) Computed angular intensity distribution after 9,700 iterations (continuous line) at radius $7 \mu\text{m}$ compared with the target distribution (dashed line). (c) Contour plot of the electric field magnitude in relative units after 9,700 iterations. (d) Evolution of the error.

FIG. 3: Comparison with a periodic structure (PC) with 56 dielectric rods ($n = 1.5$) in air. The lattice constant and the angle are chosen so that for the incident wavelength $\lambda = 1\mu\text{m}$ the Bragg diffraction condition is satisfied for 45° . (a) Positions of the cylinders and distribution of the Poynting vector field. The incident beam is propagating along the x axis (left to right). The observation circle, has a radius of $7\mu\text{m}$ and it is represented without the target window between 30 and 60 degrees. (b) Computed angular intensity distribution (continuous line) at radius $7\mu\text{m}$ compared with the target distribution (dashed line).

FIG. 4: Initial configuration for the cosine squared target function example. Si ($n = 3.5$) with 26 cylindrical holes filled with SiO_2 , TM gaussian beam incidence, beamwidth $2\sigma = 1.5\mu\text{m}$, and wavelength $\lambda = 1.5\mu\text{m}$. (a) Positions of the cylinders and distribution of the Poynting vector field. The incident beam is propagating along the x axis (left to right). The observation circle, has a radius of $6\mu\text{m}$ and it is represented without the target window between 30 and 60 degrees. (b) Computed angular intensity distribution (continuous line) at radius $6\mu\text{m}$ compared with the target distribution (dashed line).

FIG. 5: Optimized configuration for the cosine squared target function example. Si ($n = 3.5$) having 26 cylindrical holes filled with SiO_2 , TM gaussian beam incidence, beamwidth $2\sigma = 1.5\mu\text{m}$, and wavelength $\lambda = 1.5\mu\text{m}$. (a) Positions of the cylinders and distribution of the Poynting vector field. The incident beam is propagating along the x axis (left to right) after 7,000 iterations. The observation circle, has a radius of $6\mu\text{m}$ and it is represented without the target window between 30 and 60 degrees. (b) Computed angular intensity distribution after 7,000 iterations (continuous line) at radius $6\mu\text{m}$ compared with the target distribution (dashed line). (c) Contour plot of the magnetic field magnitude in relative units after 7,000 iterations. (d) Evolution of the error as a function of iteration number.

FIG. 6: Comparison between 3D and 2D simulations. (a) The 3D structure simulated and the modal field of the input ridge waveguide. The thickness of the Si slab in the 3D simulation is $0.6 \mu\text{m}$ and the (horizontal) mode size of the ridge waveguide is approximately $w = 1.5 \mu\text{m}$, the diameter of the holes is $d = 0.4 \mu\text{m}$. Incident light is TE polarized and has wavelength $\lambda = 1.5 \mu\text{m}$. (b) 3D Simulation results showing the Poynting vectors field in the middle horizontal section of the Si slab. (c) Comparison between the angular intensity distribution for the 3D and 2D simulations. (d) 2D simulation results, the Poynting vectors field.

FIG. 7: Sensitivity analysis with respect to the frequency of the incident light for the optimized structure from Fig. 5. Percentage change in error when the frequency of the light is modified from the original value $f_0 = 200 \text{ THz}$.

FIG. 8: Sensitivity analysis with respect to position for the optimized structure from Fig. 5. The 10 most sensitive cylinders are randomly moved along the x and y axis by a fixed length step (horizontal axis 10, 20, 30, 40 and 50 nm). The errors for 10 different randomly generated moved distributions are plotted for each step size.

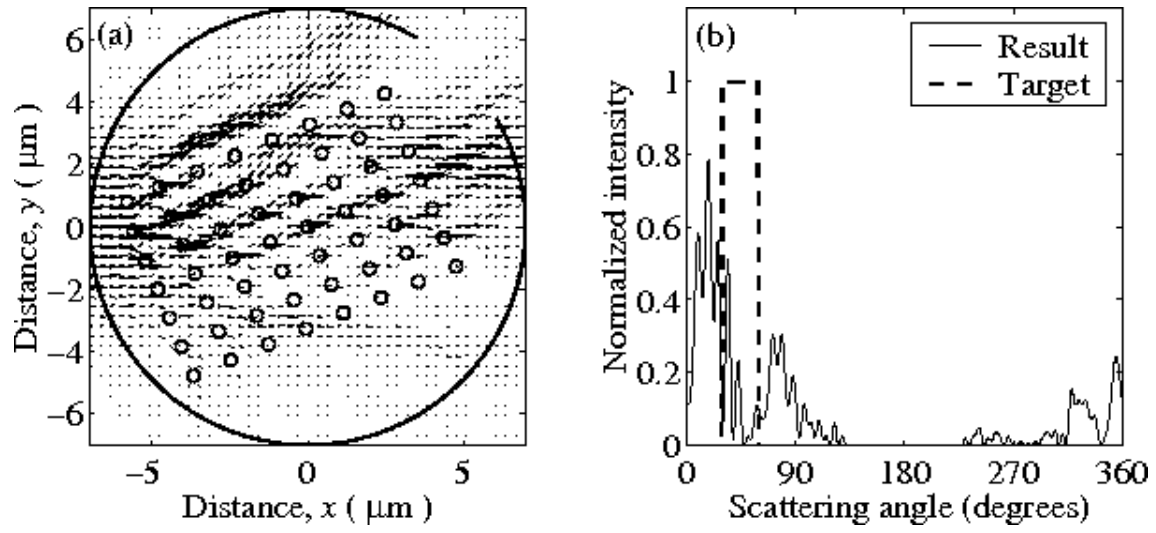


Fig. 1

Gheorma, Haas, Levi

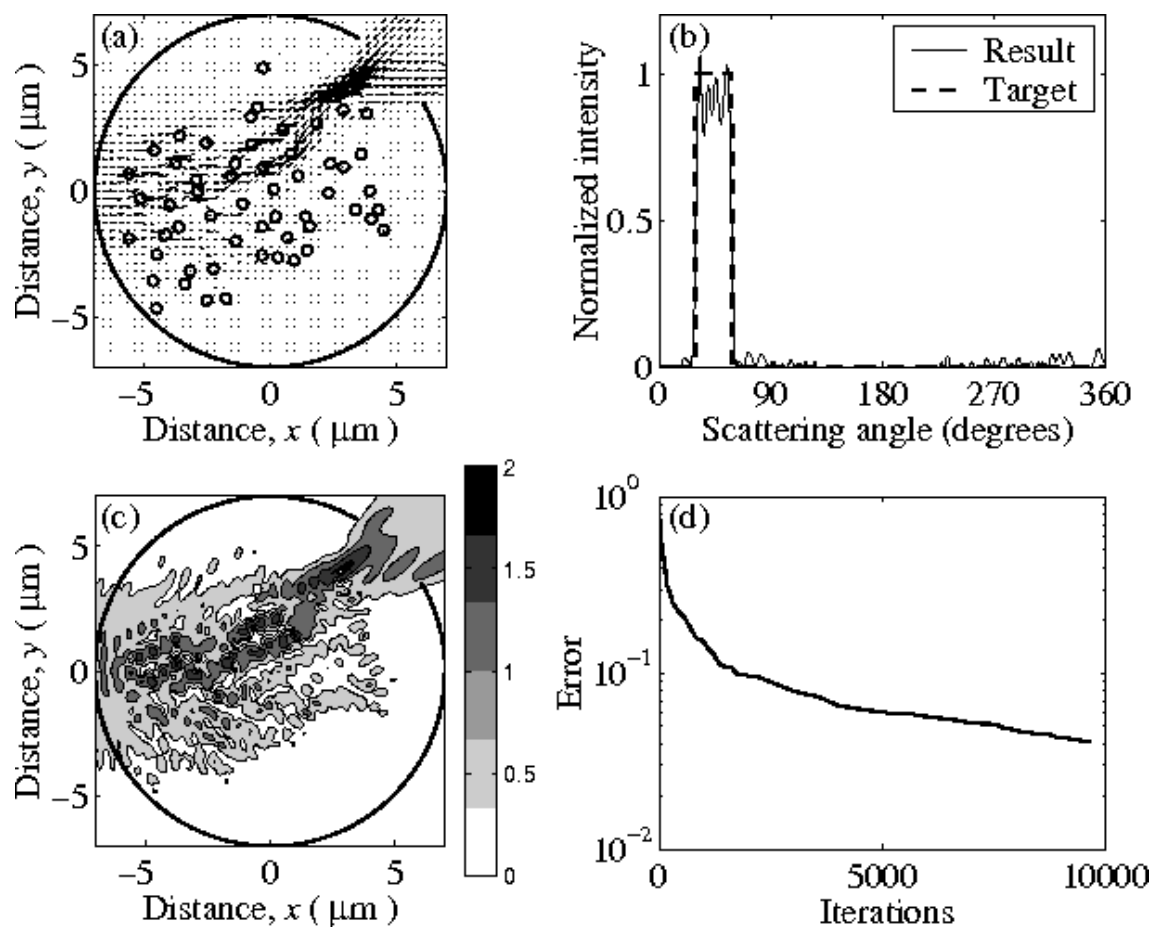


Fig. 2

Gheorma, Haas, Levi

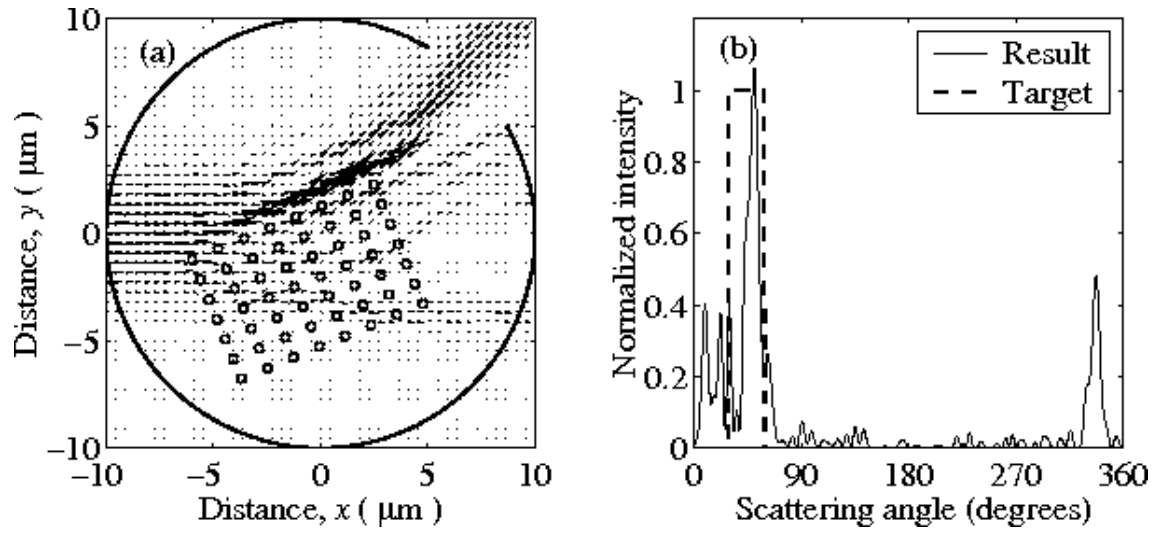


Fig. 3

Gheorma, Haas, Levi

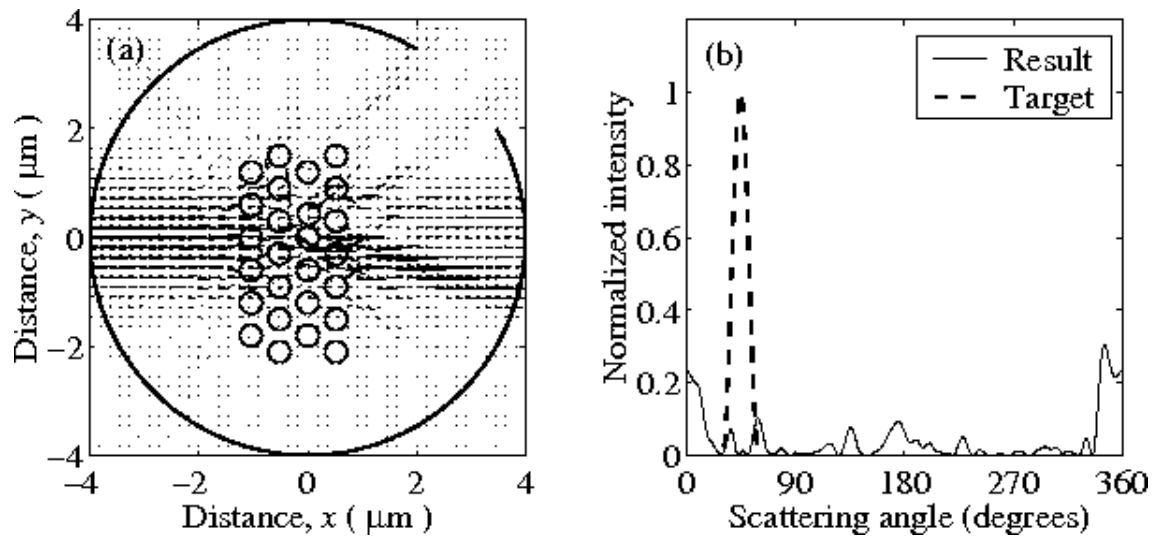


Fig. 4

Gheorma, Haas, Levi

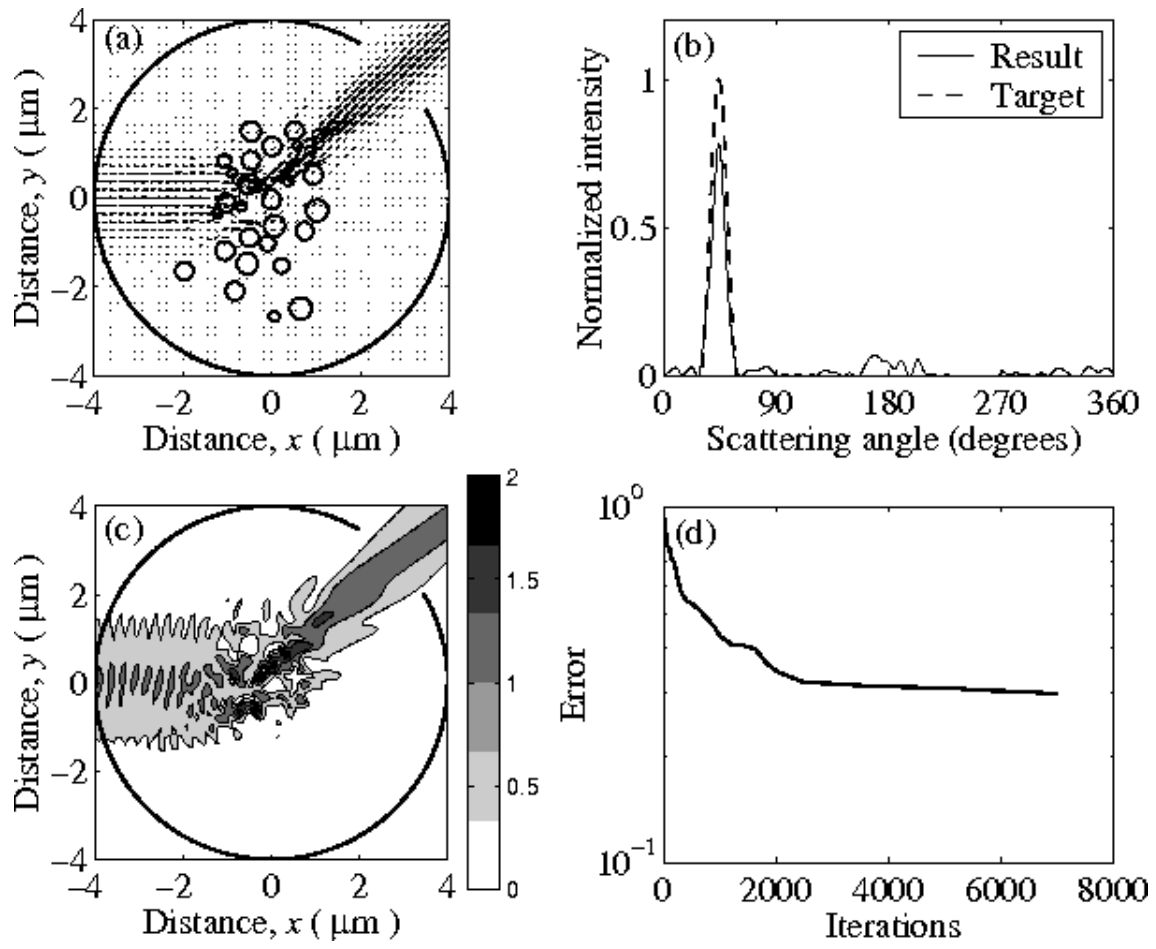


Fig. 5

Gheorma, Haas, Levi

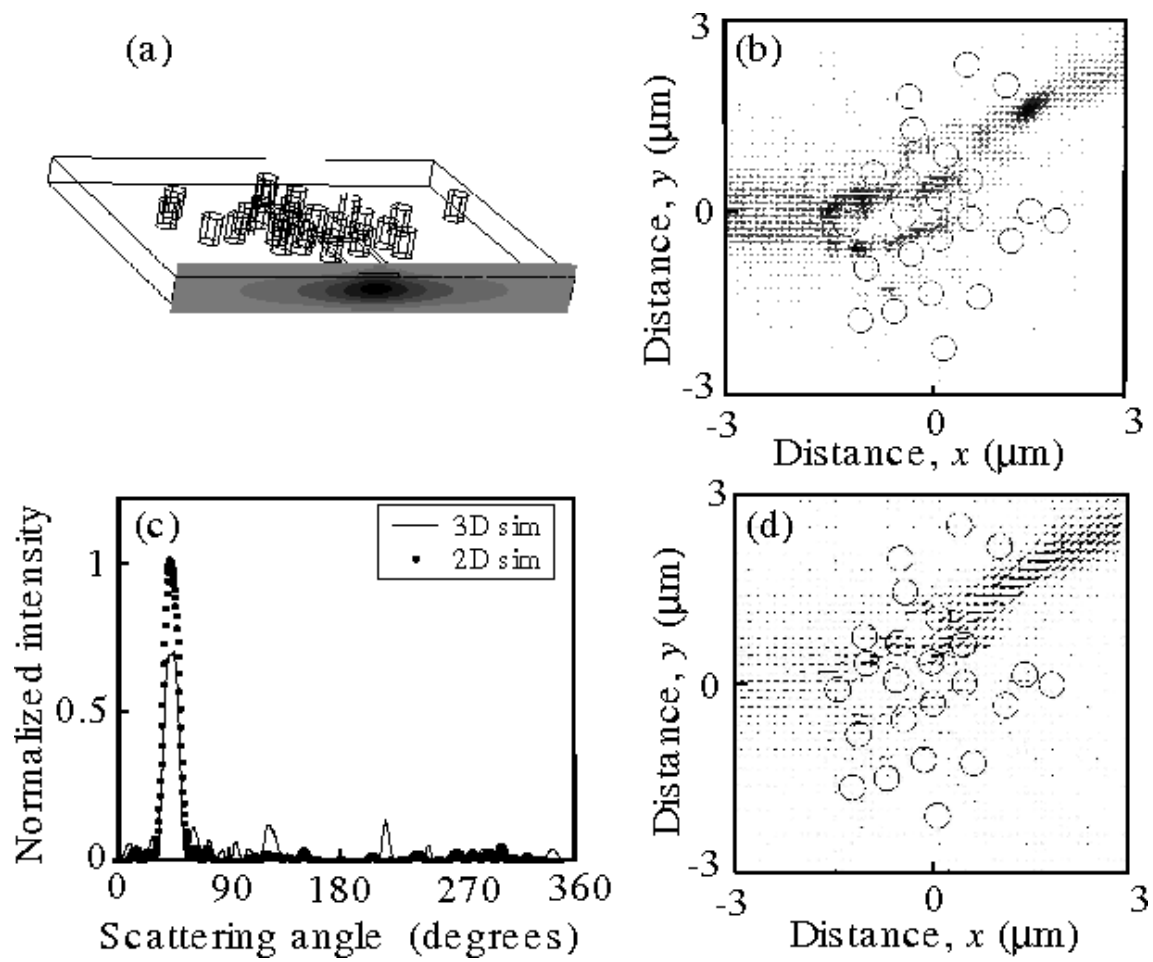


Fig. 6
Gheorma, Haas, Levi

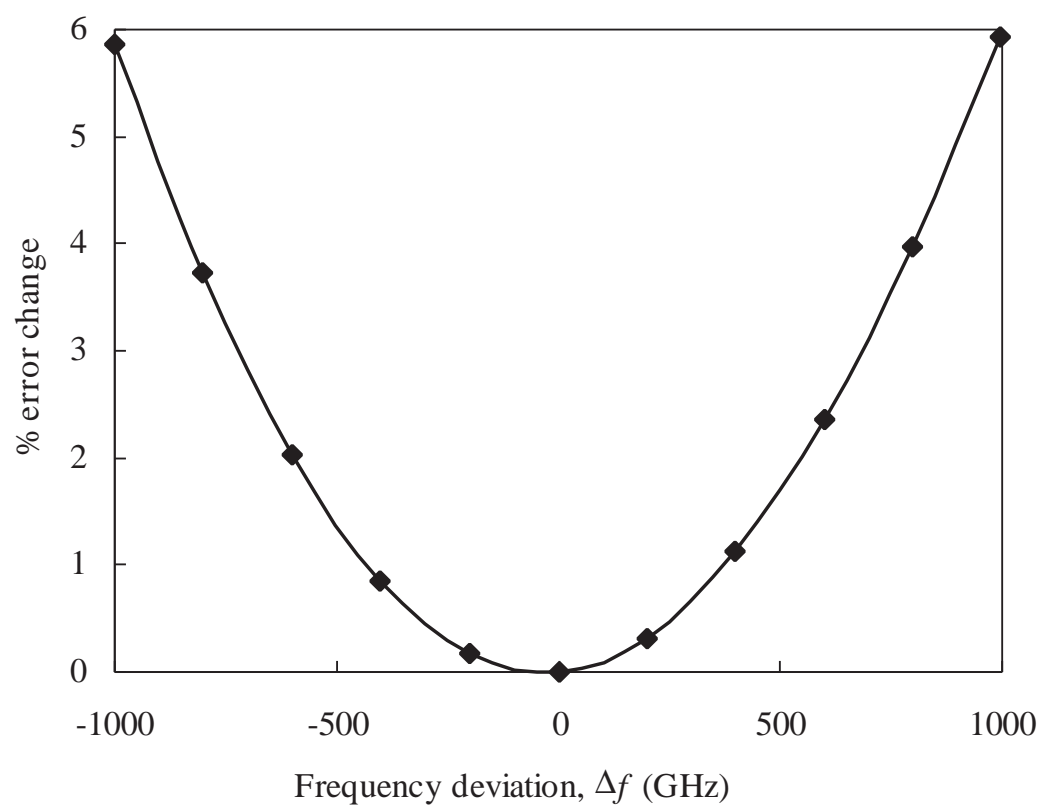


Fig. 7

Gheorma, Haas, Levi

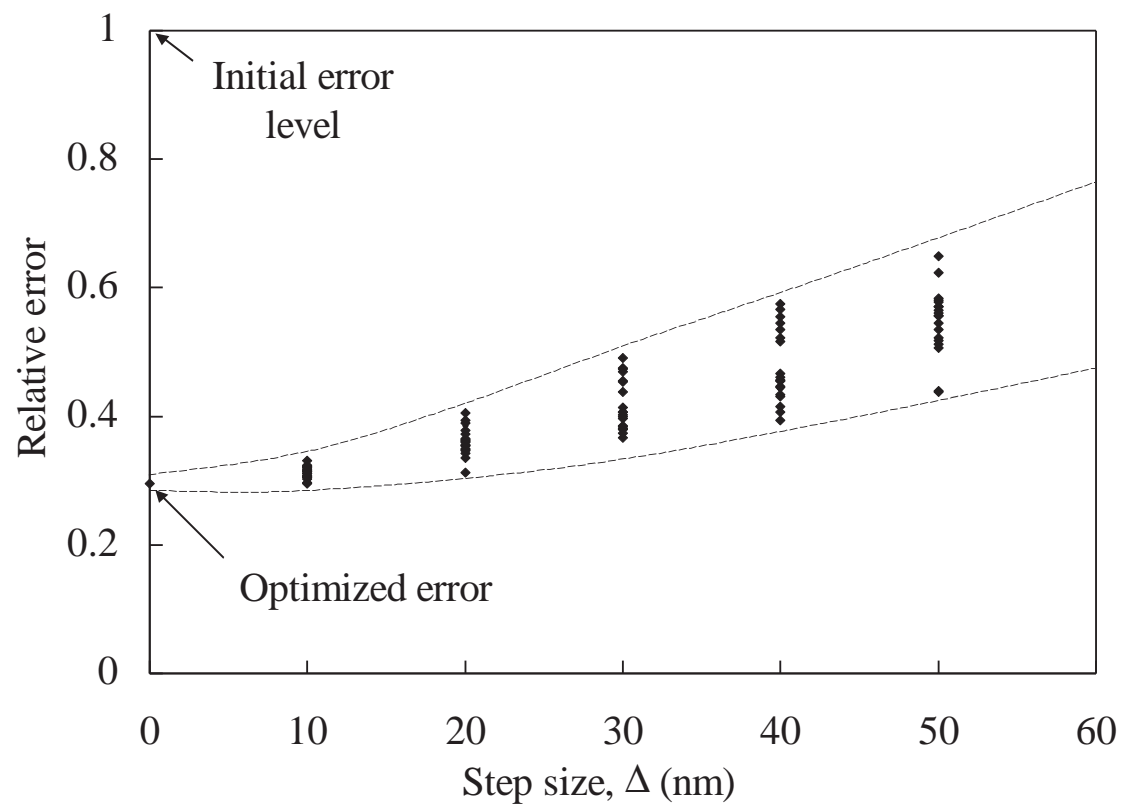


Fig. 8

Gheorma, Haas, Levi